High Redshift γ–ray Bursts:

GRB 090423 and GRB 090429B

Nuclear and Subnuclear Astrophisics

Alberto Bonollo

April 5th, 2019

Importance of high redshift GRBs

- Distant regions equal distant times;
- Star formation and population III stars.
- Studies of metallicity and absorption;
- Independence from the galaxy brightness;
- Dark matter and gravitational collapse.

But the problems are:

- Rarity of events;
- Galactic absorption.

GRB 090423

It is a double peaked, highly energetic burst with a redshift of $z=8.1$.

$T_{90} = (10.3 \pm 1.1)\,\mathrm{s}$

$E_p = 48\,\mathrm{keV}$

$T_{90,rf} = (1.13 \pm 0.12)\,\mathrm{s}$

$E_{p,rf} = 437\,\mathrm{keV}$

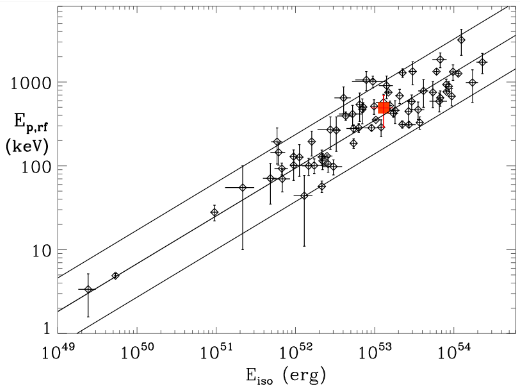

Supplementary Fig. 2. Isotropic energy and peak energy correlation. Position of GRB 090423 in the $E_{p,rf}$ – E_{iso} plane based on Swift/BAT[4] and Fermi/GBM[10] (fitted with the Band function) results. The lines show the best–fit power–law and the $\pm 2\sigma$ region of the correlation as derived by [13]. Also shown are the 70 GRBs included in the sample analyzed in that work (errors on individual bursts are at 1σ level). Given that short GRBs do not follow the correlation[13], this evidence supports the hypothesis that, despite its cosmological rest–frame duration of ~ 1.3 s, GRB 090423 belongs to the long GRB class.

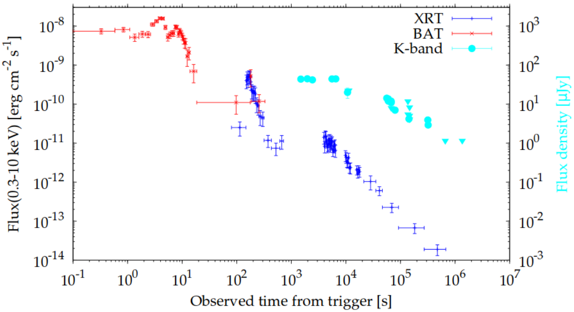

Supplementary Fig. 3. Observed light curve. Light curve of GRB 090423 as observed by Swift/BAT (red crosses), Swift/XRT (blue plus) and in the NIR (cyan points). Errors on fluxes are at 1σ level and horizontal bars refer to the integration time interval. The XRT 0.3–10 keV light-curve, starting at 73 s after the burst, shows a prominent flare at $t \sim 170$ s (also detected by BAT), and a flat phase ($\alpha_{X,1} = 0.13 \pm 0.11$) followed by a rather typical decay (starting at $t = 4513 \pm 491$ s) with power-law index $\alpha_{X,2} = 1.3 \pm 0.1$. Available photometric data are plotted in the K band (AB magnitude) by transforming the fluxes, when the observations have been taken in a different filter, using a power law with $\beta = 0.4$, as estimated from the NIR spectral energy distribution. A small displacement in time for contemporary data in different bands is applied in order to increase the visibility. The NIR light curve is consistent with a plateau phase ($t \sim 10^2 - 10^3$ s) followed by a decay with $\alpha_O \sim 0.5$ ($t \sim 10^3 - 10^5$ s). This decay phase is shallower than the X-ray decay in the same time interval. Triangles at $t \sim 10^5$ s report NIR upper limits as obtained by our second epoch TNG observation with the NICS camera in the Y and J band and by GROND in the JHK band. These limits are consistent with the temporal decay observed by XRT.

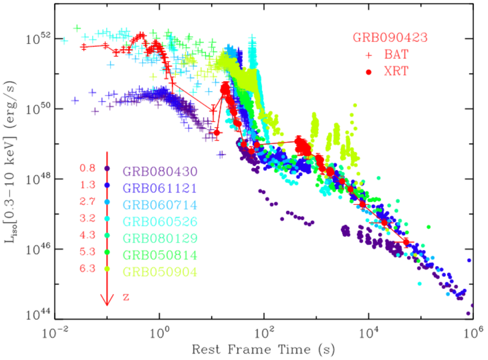

Figure 1. Rest-frame γ-ray and X-ray light curves for bursts at different redshifts. BAT and XRT light curve of GRB 090423 (red data) in the source rest-frame. Errors on luminosity, L_{iso}, are at 1σ level; horizontal bars refer to the integration time interval. The XRT 0.3–10 keV light-curve shows a prominent flare at a rest-frame time of $t_{rf} \sim 18$ s (also detected by BAT), and a flat phase (with a power-law index of $\alpha_{X,1} = 0.13 \pm 0.11$) followed by a rather typical decay with power-law index $\alpha_{X,2} = 1.3 \pm 0.1$. We compare the light curve of GRB 090423 with those of seven GRBs in the redshift interval 0.8-6.3. The bursts are selected from among those showing a canonical three-phase behaviour (steep decay/plateau/normal decay) in the X-ray light curve and without a spectral break between BAT and XRT, allowing the spectral calibration of the BAT signal into the 0.3-10 keV energy band. The light curve of GRB 090423 does not show any distinguishing features relative to those of the lower-redshift bursts, suggesting that the physical mechanism that causes the GRB and its interaction with the circumburst medium are similar at $z \sim 8.1$ and at lower redshifts.

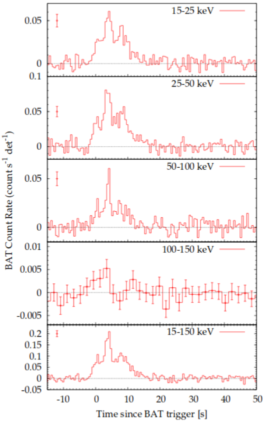

Supplementary Fig. 1. BAT mask-weighted light curve. Four channels and combined 0.512 s mask-weighted light curve. The light curve of the 100-150 keV energy channel shows a weak signal, because of the soft spectrum; the corresponding integration time is 2.048 s. Errors are at 1σ level.

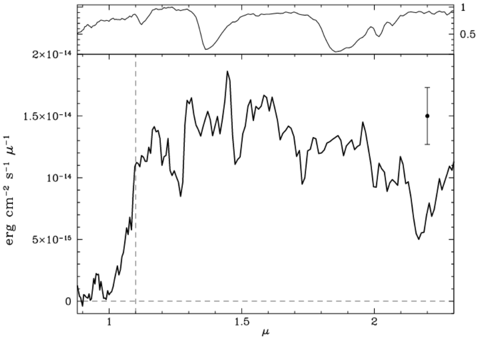

Figure 2. TNG spectrum of the NIR afterglow. Bottom Panel. Spectrum of GRB 090423 obtained using the Amici prism on the Telescopio Nazionale Galileo (TNG). The sharp break at wavelength $\lambda \approx 1.1\ \mu$m, which is due to the HI absorption in the intergalactic medium at the wavelength of the Lyα line, implies that $z = 8.1^{+0.1}_{-0.3}$. The spectrum has been smoothed with a boxcar filter of width $\Delta = 25$ pixels (where one pixel corresponds to $\sim 0.006\ \mu$m at $\lambda = 1.1\mu$m). The absolute flux calibration was obtained by matching the almost simultaneous GROND photometric measurements[7]. The wavelength calibration was obtained from the TNG archive and adjusted to the wavelengths of the main atmospheric bands. The error bar corresponds to $\pm 1\sigma$ uncertainty as measured on the smoothed spectrum. The confidence level of the Lyman-α break detection is $\gtrsim 4\sigma$. See also Supplementary Information, section 3. Top Panel. Plot of the trasmittance (the atmospheric transparency convolved with the instrumental response). The system has a significant sensitivity down to 0.9 μm, and no instrumental or atmospheric effect could explain the abrupt flux break observed in the spectrum of GRB 090423.

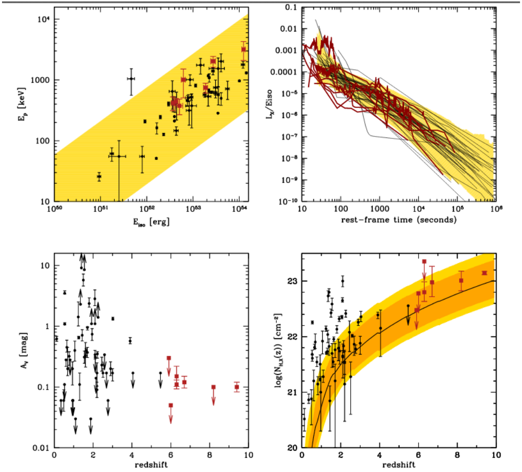

Figure 1: Comparison of the properties of $z > 6$ bursts (red squares and lines) with those of a well selected complete sub-sample of bright *Swift* GRB, the BAT6 sample (black points and lines; Salvaterra et al. 2012). *Top-left panel*: $E_p - E_{iso}$ correlation where BAT6 bursts are from Nava et al. (2012). The shaded regions represents the 3σ scatter around the best-fitting relation. *Top-right panel*: rest-frame 2-10 keV light curves normalized to their isotropic energy where BAT6 data are from D'Avanzo et al. (2012). The shaded region represents the 2σ scatter around the mean value of the L_X/E_{iso} distributions at the given rest-frame time. *Bottom-left panel*: dust extinction as a function of redshift, where BAT6 data are from Covino et al. (2013). *Bottom-right panel*: intrinsic X-ray equivalent hydrogen column densities $N_{H,X}$ as a function of redshift, where BAT6 data are from Campana et al. (2012). The shaded regions represent the effect of intervening material along the line-of-sight (see Campana et al. 2015 for the details).

GRB 090429B

It is a highly energetic burst with a redshift of z=9.4 .

$T_{90} = 5.5\,s$

$T_{90,rf} = 0.5\,s$

$E_p = 49\,keV$

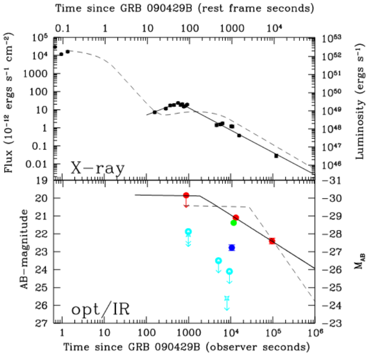

Fig. 1.— X-ray (top) and optical/IR (bottom) lightcurve of GRB 090429B, the left-hand and bottom axis represent the observed time and flux/magnitude, while the top and right-hand axis show rest-frame time and luminosity, respectively. The solid points in the top panel show the observed XRT data, along with a solid line representing the model. The dashed line represents the best fit model for GRB 090423 (Tanvir et al. 2009) overplotted as it would appear at $z \sim 9.4$. The lower panel shows the optical lightcurve, along with a single power-law fit to the (red) K-band points. (H and J are shown as green and blue, respectively. For clarity we have shown only the i- and z-band limits (cyan) in the optical). Additionally, the dashed line again shows the model of GRB 090423 at $z \sim 9.4$. As can be seen, the luminosity and general behavior of GRB 090429B in both X-ray and optical is similar to that of GRB 090423.

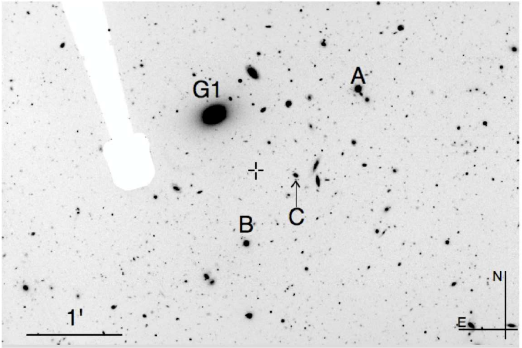

Fig. 4.— Wide-field image of the GRB 090429B field, obtained with Gemini-North 14 days after the burst. The location of the GRB is marked with a crosshair. Additionally, we mark the positions of the three comparison stars used to refine our photometry (note that star C is faint, and lies at the end of the marked arrow, just to the south of the galaxy), and the location of a large elliptical galaxy (G1), which is the central galaxy of a modest cluster at $z \approx 0.08$, which may provide a modest lensing magnification. Note the silhouette of the guide probe obscures part of the field.

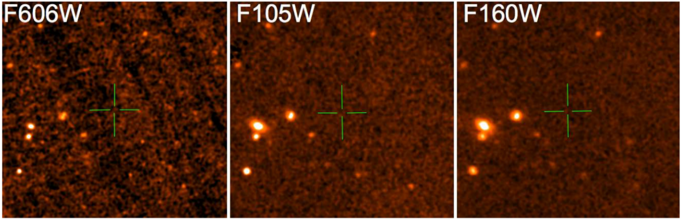

Fig. 10.— Our late time *HST* observations of the GRB 090429B field in the optical and NIR. No host galaxy is detected in any filter, supporting a high-redshift origin, since a host with $z < 1$ would be very unlikely to be fainter than these limits, even if dusty. At $F160W$ the host remains undetected, but the observations reach limits which would uncover $\sim 50\%$ of the $z > 8$ candidates in the Hubble Ultra-Deep Field (UDF). Hence, the non-detection of any host is fully consistent with our high-z model, but inconsistent with any lower redshift, high extinction scenario.

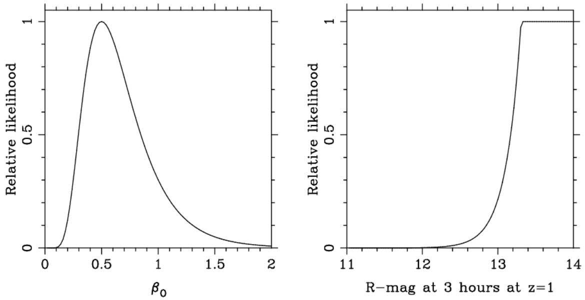

Fig. 5.— Input priors adopted for our photometric redshift fitting. [Left panel:] In the relativistic fireball model, the intrinsic spectral slope in the optical should lie between β_X and $\beta_X - 0.5$ (plus the associated measurement errors). To achieve this we use a lognormal distribution centered at 0.5 (since there does appear to be a break between the optical and X-ray, see Figure 3). This is a relatively weak prior and simply avoids extreme values of β. Right panel: The second prior is on the intrinsic optical afterglow luminosity, and impacts solutions that would result in an unreasonably bright luminosity (it is not bounded at the faint end, and hence the low-redshift solutions are unaffected). It is therefore based on the empirically observed upper envelope of afterglow luminosities. The primary impact of this prior is to disfavor moderate ($A_V > 3$) scenarios at high redshift ($z > 7$), where the burst would have been more luminous than any other known afterglow.

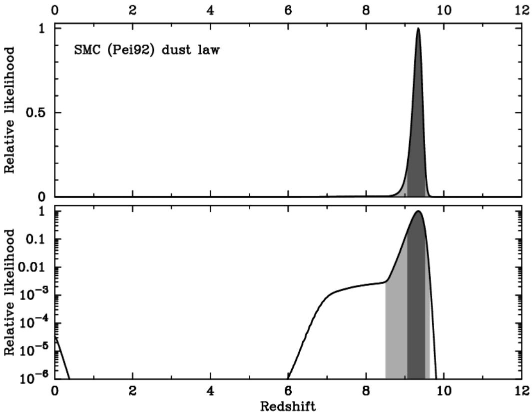

Fig. 9.— Posterior likelihood plotted on both a linear (upper) and log (lower) scale, for the models assuming an SMC dust law, where we have marginalized over both α (assumed to have a flat prior between -1 and $+1$) and A_V (assumed to have a flat prior between 0 and 12). The dark and light shaded bands show the extent of the 90% and 99% enclosed likelihood regions respectively.

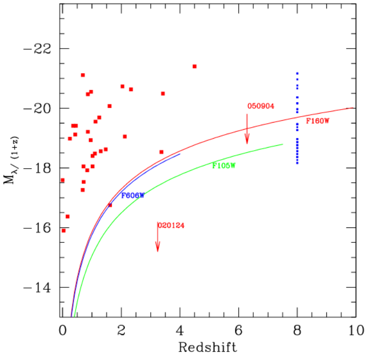

Fig. 11.— Solid lines show the 3σ absolute magnitude limits for GRB 090429B in each of our filters *F606W* (blue), *F105W* (green) and *F160W* (red). The inferred absolute magnitudes (AB) of a sample of GRB host galaxies (Fruchter et al. 2006), as a function of redshift (plot modified from Perley et al. 2009). The known GRB hosts with *HST* observations are plotted as red points, and are supplemented at high redshift by the observations of GRB 050904 by Berger et al. (2006). As can be seen, all of these lines lie significantly below the majority of GRB hosts and offer support for a high-redshift origin for GRB 090429B. The blue points at $z \sim 8$ represents the Lyman break sample of Bouwens et al. (2010). As can be seen, the limiting magnitude for GRB 090429B lies roughly at the median of this distribution, and so the non-detection in our observations would not be unexpected at $z \sim 9.4$

General considerations

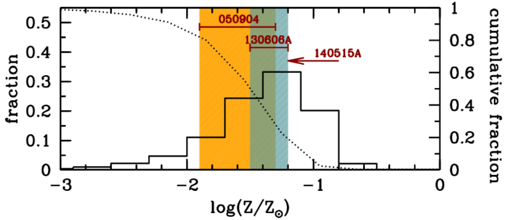

Figure 3: Properties of simulated GRB hosts in the redshift range $z = 6 - 10$. Panels from top to bottom show the distribution of UV absolute magnitude, of the SFR (in $M_\odot$ yr^{-1}), and of gas phase metallicities (in solar units). The dotted line shows the normalized cumulative distributions (see right y-axis). The arrows in the first two panels report the limits on M_{UV} and SFR of GRB hosts (Tanvir et al., 2012). The shaded areas in the bottom panel correspond to the metallicity measured in the GRB 050904 (Thöne et al., 2013) and GRB 130606A (Hartoog et al., 2014) afterglow spectrum. The arrow shows the limit inferred for GRB 140515A (Chornock et al., 2014).

Redshift distribution models

Observing the spectrum we can put limits on the metallicity ($Z = 0.043 Z_\odot$) and model the redshift distribution:

- No evolution model
- Luminosity evolution model
- Density evolution model

Model distribution is calculated through photon flux:

$$P = \int_{(1+z)E_{min}}^{(1+z)E_{max}} (S(E)/4\pi d^2) dE$$

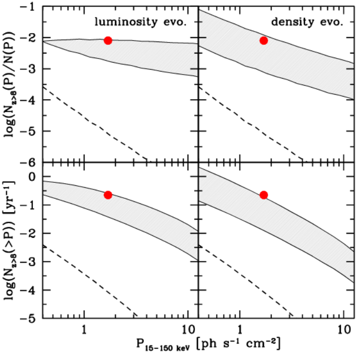

Supplementary Fig. 6. Probability of the occurance of GRB 090423. Top panels: probability for a GRB with peak photon flux P to be detected by Swift at $z \geq 8$. Luminosity evolution models are shown in the left panel, where shaded area refers to a typical burst luminosity increasing as $L_{\rm cut} \propto (1+z)^{\delta}$ with $\delta = 1.5 - 3$. Density evolution models are shown in the right panel, where shaded area refers to a metallicity threshold for GRB formation $Z_{th} = 0.02 - 0.2\ Z_{\odot}$ (the lower bound refers to the higher Z_{th}). In both panels, the dashed line shows the no evolution case. The red point marks the position of GRB 090423. We note that the point represents a lower limit on the number of detection at $z > 8$ since a few very high-z bursts may be hidden among those bursts that lack of an optical detection. Bottom panels: cumulative number of GRBs at $z > 8$ to be detected by Swift with photon flux larger than P in one year of Swift observations.

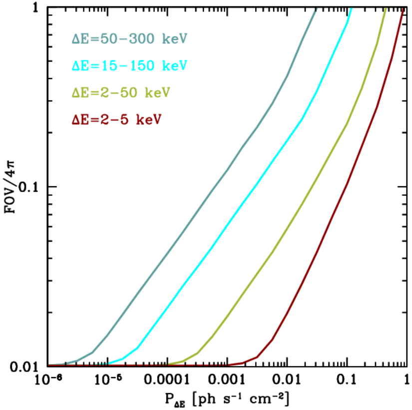

Figure 4: Required sensitivity, in terms of minimum peak flux $P_{\Delta E}$ that can be detected in the given energy band ΔE, and field-of-view to detect 10 GRB yr^{-1} at $z > 8$. Different lines correspond to different energy bands as labeled in the plot, i.e. to different mission concept. See Ghirlanda et al. (2015) for the details of the calculation.